Structural characterization of precious-mean quasiperiodic Mo/V single-crystal superlattices grown by dual-target magnetron sputtering

J. Birch, M. Severin, U. Wahlström, Y. Yamamoto,* G. Radnoczi,† R. Riklund, and J.-E. Sundgren
Department of Physics and Measurement Technology, Linköping University, S-581 83 Linköping, Sweden

L. R. Wallenberg
National Center for High Resolution Electron Microscopy, Chemical Center, University of Lund, P.O. Box 124, S-221 00 Lund, Sweden
(Received 8 December 1989)

A class of quasiperiodic superlattice structures, which can be generated by the concurrent inflation rule $A \rightarrow A^m B$ and $B \rightarrow A$ (where m=positive integer), has been studied both theoretically and experimentally. Given that the ratios between the thicknesses of the two superlattice building blocks, A and B, are chosen to be $\gamma(m)=[m+(m^2+4)^{1/2}]/2$ (known as the "precious means"), then the x-ray- and electron-diffraction peak positions are analytically found to be located at the wave vectors $q=2\pi\Lambda^{-1}r[\gamma(m)]^k$, where r and k are integers and Λ is an average superlattice wavelength. The analytically obtained results have been compared to experimental results from single-crystalline Mo/V superlattice structures, generated with $m=1$, 2, and 3. The superlattices were grown by dual-target dc-magnetron sputtering on MgO(001) substrates kept at 700 °C. X-ray diffraction (XRD) and selected-area electron diffraction (SAED) showed that the analytical model mentioned above predicts the peak positions of the experimental XRD and SAED spectra with a very high accuracy. Furthermore, numerical calculations of the diffraction intensities based on a kinematical model of diffraction showed good agreement with the experimental data for all three cases. In addition to a direct verification of the quasiperiodic modulation, both conventional and high-resolution cross-sectional transmission electron microscopy (XTEM) showed that the superlattices are of high crystalline quality with sharp interfaces. Based on lattice resolution images, the width of the interfaces was determined to be less than two (002) lattice-plane spacings ($\approx$0.31 nm).

I. INTRODUCTION

Artificial superlattices are a new class of materials, usually prepared by alternately depositing very thin (<10 nm) layers of two constituent materials. In this way a film with a compositional modulation along the growth direction can be formed. These new materials have been shown to exhibit unusual behavior of many physical properties, depending on the layer thicknesses of the superlattice. For example, anomalies in lattice spacings,[1-3] elastic moduli,[1,3] and electrical resistivity,[1,4] extreme hardness,[5] increased critical fields in superconductors,[6] and quantum phenomena in semiconductors[7] have been reported. Consequently the interest in superlattices has increased rapidly during the past few years.

Normally the modulation is chosen to be periodic, but in recent years much interest in superlattices with an aperiodic layer sequence has evolved.[8] This interest stems partly from the discovery of quasicrystals in 1984 by Shechtman *et al.*[9] Although quasicrystals are perfectly ordered, they cannot be described in the usual terms of Bravais lattices or periodic spacing of unit cells (because they lack translational invariance) and Bloch's theorem is thus inapplicable. Instead these quasicrystals are quasiperiodic,[10] i.e., they have a deterministic aperiodic order and they can be regarded as an intermediate case between periodic and disordered solids. Since the three-dimensional quasicrystals are very complex, it can be advantageous to study one-dimensional quasiperiodic structures, e.g., superlattices, in order to gain more insight into the physical properties of quasicrystalline materials.

Merlin *et al.*,[11] using molecular-beam epitaxy, produced the first quasiperiodic superlattice in 1985 by alternating thin GaAs and AlAs layers in a composite structure whose layer counts follow the Fibonacci sequence. Since then, several experiments on superlattices based on this sequence have been reported including one paper concerning superconductivity of the Mo/V system.[12] The Fibonacci sequence can be obtained by repeated applications of the concurrent substitution rules $A \rightarrow AB$ and $B \rightarrow A$, so that in successive generations we get, $A \Rightarrow AB \Rightarrow ABA \Rightarrow ABAAB \Rightarrow ABAABABA \Rightarrow \cdots$, etc. Although theoreticians have paid most attention to the Fibonacci sequence, several other quasiperiodic sequences have also been studied.[8,13-17] However, to our knowledge, all experiments up to now except one,[18] in which a Thue-Morse[17] sequence was grown, have been constituted as Fibonacci superlattices. Since superlattices with different quasiperiodic modulations have been predicted to exhibit different physical properties,[13-17] it is of interest to be able to grow and characterize such various structures.

In the present work, the diffraction properties of a whole class of quasiperiodic superlattices, which can be generated by the concurrent inflation rule $A \rightarrow A^m B$ and $B \rightarrow A$, where $A^m B$ means a sequence of m basic building blocks of type A followed by the one single block of type B, have been studied both theoretically and experimentally. In the limit of an infinite superlattice, the ratios between the number of A and B blocks in these superlattices approach the irrational numbers $\gamma(m)=[m+(m^2+4)^{1/2}]/2$, known as the mth "precious means." It is well known that the Fibonacci sequence, which is based on the golden mean τ $[=\gamma(1)]$, gives rise to diffraction peaks for scattering vectors given by $q=2\pi\Lambda^{-1}r\tau^k$, where r and k are integers and Λ is an average superlattice wavelength. In Sec. II, we present a theoretical model leading to the more general analytical expression $q=2\pi\Lambda^{-1}r[\gamma(m)]^k$, which is valid for the whole class of precious-mean superlattices. After a brief description of the sputtering system, the sample preparation, and the analytical techniques in Sec. III, it is shown in Sec. IV that the as-deposited Mo/V superlattices are single crystalline with an interface width of two (002) lattice spacings (0.31 nm) and the analytical expression is verified for $m=1$, 2, and 3 by experimental x-ray-diffraction (XRD) and selected-area electron-diffraction (SAED) spectra. Furthermore, numerical calculations of the electron- and x-ray-diffraction intensities based on a kinematical model of diffraction and sharp interfaces show good agreement with the experimental data for all three cases.

II. THEORETICAL MODELS

This section briefly outlines the relevant theory used in the present work. A more thorough treatment has been presented in Ref. 14. The diffraction peak positions are in general given by the maxima of the Fourier transform of the superlattice electron density. The subject of this section is thus to write the charge density of a precious-mean superlattice in a suitable form and to find the maxima of its Fourier transform. The electron density in the growth direction of a superlattice, $\rho(z)$, can be written as

$$\rho(z)=\begin{cases}\rho_A(z), & z_{n+1}-z_n=d_A \\ \rho_B(z), & z_{n+1}-z_n=d_B\end{cases}$$
$$z_n \le z < z_{n+1}, \quad n \in \mathbb{Z}, \qquad (2.1)$$

where $\rho_{A\,(B)}(z)$ is the electron density of building blocks of type A (B) with thicknesses $d_{A\,(B)}$. For the class of sequences generated by the concurrent inflation rule $A \rightarrow A^m B$ and $B \rightarrow A$ (for m a positive integer), which is considered in the present paper, the z_n is the set of points

$$z_n = n d_B + (d_A - d_B)\left\lfloor \frac{n}{\sigma(m)} \right\rfloor, \qquad (2.2)$$

which is illustrated schematically in Fig. 1(a). The bracket notation $\lfloor\ \rfloor$ (the "floor") means the largest integer smaller or equal to the entity within the brackets, and $\sigma(m)$ is given by

$$\sigma(m)=\frac{2-m+(4+m^2)^{1/2}}{2} \quad \text{for } m=1,2,3,\ldots . \qquad (2.3)$$

The Fourier transform, $F(Q)$, of $\rho(z)$ can now be written as

$$F(Q)=F_A(Q)\sum_{\substack{n \\ (z_{n+1}-z_n=d_A)}} e^{iQz_n} + F_B(Q)\sum_{\substack{n \\ (z_{n+1}-z_n=d_B)}} e^{iQz_n}, \qquad (2.4)$$

where Q is the scattering vector and the summations run over the z_n which mark the lowest positions of A and B blocks, respectively. $F_{A\,(B)}(Q)$ is the Fourier transform

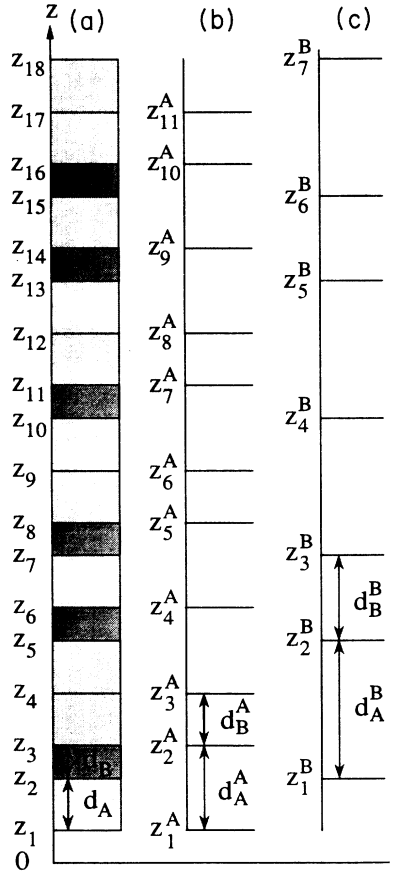

FIG. 1. Schematic representation of (a) the superlattice where $d_{A\,(B)}$ represents the thicknesses of the A and B building blocks and z_n are their positions according to Eq. (2.2). (b) and (c) show the two sublattices formed by the positions, z_n^A and z_n^B, of the A and B building blocks, respectively. The only difference between the A and B sublattices is their lattice constants $d_{A\,(B)}^A$ and $d_{A\,(B)}^B$, respectively.

of $\rho_{A(B)}(z)$

$$F_{A(B)}(Q)=\int_0^{d_{A(B)}}\rho_{A(B)}(z)e^{iQz}dz \ . \tag{2.5}$$

The two sums in Eq. (2.4) corresponds to the Laue function[19] in the periodic case and are thus the quantities that determine the positions of the superlattice satellites.

It has been shown[14] that for the class of sequences considered here, the A blocks are forming a sublattice defined by the set of points

$$z_n^A=nd_B^A+(d_A^A-d_B^A)\left\lfloor\frac{n}{\sigma^A(m)}\right\rfloor+d_B-d_A \ , \tag{2.6}$$

where

$$\begin{aligned} &d_B^A=d_A, \quad d_A^A=d_A+d_B \ , \\ &\sigma^A(m)=\gamma(m)=\tfrac{1}{2}[m+(4+m^2)^{1/2}] \ . \end{aligned} \tag{2.7}$$

We use the convention that superscript labels refer to the sublattice in question and subscript labels refer to the corresponding building block. d_B^A (d_A^A) is thus the size of the thinnest (thickest) building block in the sublattice given by the positions of the original A blocks as is shown in Fig. 1. The corresponding equations for the B layers read

$$z_n^B=nd_B^B+(d_A^B-d_B^B)\left\lfloor\frac{n}{\sigma^B(m)}\right\rfloor \ , \tag{2.8}$$

where now

$$d_B^B=d_B+md_A, \quad d_A^B=d_B+(1+m)d_A, \quad \sigma^B(m)=\gamma(m) \ . \tag{2.9}$$

Since $\sigma^A(m)=\sigma^B(m)=\gamma(m)$, Eqs. (2.6) and (2.8) imply that the A blocks of the original superlattice form a quasiperiodic lattice on its own which differs from the corresponding lattice formed by the B blocks only in the lattice constants $d_{A(B)}^A$ and $d_{A(B)}^B$, as is demonstrated in Fig. 1 for $m=1$. These lattices are, however, different from the original lattice except in the special case of the Fibonacci lattice where $m=1$.

It is now possible to rewrite Eq. (2.4) as

$$F(Q)=F_A(Q)\sum_n e^{iQz_n^A}+F_B(Q)\sum_n e^{iQz_n^B} \tag{2.10}$$

with z_n^A and z_n^B given by Eqs. (2.6) and (2.8).

It has further been shown[20] that, provided that z_n satisfies Eq. (2.2), the following relation holds:

$$\sum_n e^{iQz_n}=\sum_{l,n} e^{-iZ_{ln}}\frac{\sin(Z_{ln}/2)}{Z_{ln}/2}\delta(Q\Lambda-Q_{ln}\Lambda) \tag{2.11}$$

where

$$\begin{aligned} &Q_{ln}=\frac{2\pi}{\Lambda}\left\lfloor n+\frac{l}{\sigma}\right\rfloor \ , \\ &Z_{ln}=\frac{2\pi}{\Lambda}[n(d_A-d_B)-ld_B] \ , \\ &\Lambda=d_B+\frac{d_A-d_B}{\sigma} \ , \end{aligned} \tag{2.12}$$

and l and n are integers; Λ is called the quasiperiodic wavelength. The maxima of (2.11) will then occur for $Q=Q_{ln}$ such that $Z_{ln}=0$.

Now, defining the generalized Fibonacci numbers $F_k^{(m)}$ as

$$F_{k+1}^{(m)}=mF_k^{(m)}+F_{k-1}^{(m)} \quad \text{for } k\geq 1 \ ,$$

$$\text{with } F_0^{(m)}=0 \text{ and } F_1^{(m)}=1 \ , \tag{2.13}$$

the following relation holds:[14]

$$\gamma^k=F_k\gamma+F_{k-1} \tag{2.14}$$

and it can be shown that the kth rational approximant to γ is given by F_k/F_{k-1}. Further, given that d_A and d_B are chosen such that

$$d_A/d_B=\gamma \tag{2.15}$$

it is possible to rewrite the equations corresponding to (2.12) for the two sums in Eq. (2.10) as

$$\begin{aligned} &Q_{ln}^A=\frac{2\pi}{\Lambda^A}\left\lfloor n+\frac{l}{\gamma}\right\rfloor \ , \\ &Z_{ln}^A=\frac{2\pi}{\Lambda^A}d_B(n-l\gamma) \ , \\ &\Lambda^A=d_B(\gamma+1/\gamma) \ , \end{aligned} \tag{2.16}$$

and

$$\begin{aligned} &Q_{ln}^B=\frac{2\pi}{\Lambda^B}\left\lfloor n+\frac{l}{\gamma}\right\rfloor \ , \\ &Z_{ln}^B=\frac{2\pi}{\Lambda^B}d_B(n-l\gamma)\gamma \ , \\ &\Lambda^B=d_B(\gamma^2+1) \ . \end{aligned} \tag{2.17}$$

The condition $Z_{ln}^{AB}\approx 0$ now reduces to $n=rF_k$ and $l=rF_{k-1}$ with r and k being integers. Applying this to Eqs. (2.16) and (2.17) and using Eq. (2.14) then leads to the following relation for superlattice peak positions, i.e., for the positions of the peaks of the two sums in Eq. (2.10):

$$Q_{kr}^{A,B}=\frac{2\pi}{\Lambda^{A,B}}\frac{r}{\gamma}(F_k\gamma+F_{k-1})=\frac{2\pi}{\Lambda^{A,B}\gamma}r\gamma^k, \quad r,k\in\mathbb{Z} \ . \tag{2.18}$$

Finally, noting that $\Lambda^B=\gamma\Lambda^A$, we conclude that for $d_A/d_B=\gamma$ the sums in (2.10) have peaks at the *same* Q values $Q_{k,r}$ given by

$$Q_{k,r}=\frac{2\pi}{\Lambda^B}r\gamma^k, \quad r,k\in\mathbb{Z} \ . \tag{2.19}$$

It can be seen from Eqs. (2.16) and (2.17) that if $Q_{k,r}$ and $Q_{k',r'}$ are two superlattice peak positions according to (2.19), then the wave vectors $Q=Q_{k,r}\pm Q_{k',r'}$ will also satisfy $Z_{ln}^{AB}\approx 0$ and thus give rise to diffraction peaks, as is also shown experimentally by both XRD and SAED in Sec. IV.

The numerical calculations of the diffraction spectra

shown in Sec. IV have been obtained by applying a kinematical model where the scattered intensity $I(Q)$ is given by the relation

$$I(Q)=\left|\sum_n f_n \exp(iQz_n)\right|^2 , \tag{2.20}$$

where the summation now runs over the atomic planes at positions z_n and the scattering factor f_n for each plane is assumed to be Q-independent and proportional to the atomic number N_n of the element occupying the plane in the case of x-ray diffraction and proportional to $N_n^{2/3}$ for electron diffraction. Furthermore, the interfaces are assumed to be sharp, i.e., all atoms in a certain plane n are taken to be either Mo or V atoms.

To summarize this section we conclude that if the tile sizes in a precious-mean superlattice are chosen such that $d_A/d_B=\gamma$, the superlattice peak positions can be labeled by two integers $[{}^k_r]$ which are given by Eq. (2.18). Linear combinations of these Q values will also correspond to diffraction peaks, labeled $[{}^k_r]+[{}^{k'}_{r'}]$.

III. SAMPLE PREPARATION AND ANALYSES

Single-crystalline Mo/V superlattices were grown epitaxially on (001)-oriented MgO substrates. The films were grown in a diffusion pumped sputtering system, with an ultimate pressure of 2×10^{-7} Torr (2.7×10^{-5} Pa), equipped with two circular dc planar magnetron cathodes (with diameter $=50$ mm) directed towards the substrate. In order to create the quasiperiodic modulations of the superlattices with as high accuracy as possible, two individually computer-controlled shutters, one for each magnetron, were used. The computer control together with a pneumatic operation of the shutters made it possible to control the deposition time for each layer with an accuracy of 0.1 s. In order to reduce intermixing in the interfaces, the opening of one shutter was delayed by 0.25 s after closing the other. A more detailed description of the deposition system is given in Ref. 21.

The freshly cleaved MgO substrates were, after being blown free from dust with dry N_2, immediately inserted into the vacuum chamber and placed on a tantalum plate, which could be heated resistively. When the pressure was lower than 2×10^{-6} Torr (2.7×10^{-4} Pa) the substrates were annealed at 800 °C for 1 h in order to produce as clean and well ordered a substrate surface as possible. [This method has been shown to give a good (1×1) low-energy electron-diffraction pattern in an ultrahigh-vacuum system.] Before the deposition was initiated, the substrate temperature was lowered to 700 °C and the targets were sputter cleaned for 5 min with the shutters in closed position. The pressure of argon (99.9997%) was kept constant at 6×10^{-3} Torr (0.8 Pa) during sputtering. The temperature was measured through a boron-silicate window by using an infrared pyrometer. It was calibrated to a Chromel-Alumel thermocouple placed in a hollow MgO dummy substrate covered with a thin film of Mo and placed at the substrate position. The pyrometer reading was not found to be affected by the plasma at the temperatures of interest.

The deposition rates were determined by growing two periodic superlattices with different ratios between the deposition times of the individual Mo and V layers. The rates were then calculated from the equations

$$r_V t_{1V}+r_{Mo}t_{1Mo}=\Lambda_1 , \tag{3.1a}$$

$$r_V t_{2V}+r_{Mo}t_{2Mo}=\Lambda_2 , \tag{3.1b}$$

where r_V and r_{Mo} are the deposition rates of V and Mo, respectively, t is the shutter opening time, and the subscripts 1 and 2 denote the different superlattices. The superlattice period Λ was determined from the superlattice satellite peak positions in x-ray-diffraction spectra. The deposition rates were found to be 1.6 Å/s for Mo and 1.3 Å/s for V at target voltages and currents of 350 V and 0.3 A and 290 V and 0.7 A, respectively.

The computer program controlling the superlattice modulation during growth is capable of generating any periodic or quasiperiodic sequence expressible by the 2×2 matrix formalism described by Ref. 22. In the present work the quasiperiodic sequences have generation matrices of the form

$$\begin{bmatrix} m & 1 \\ 1 & 0 \end{bmatrix} ,$$

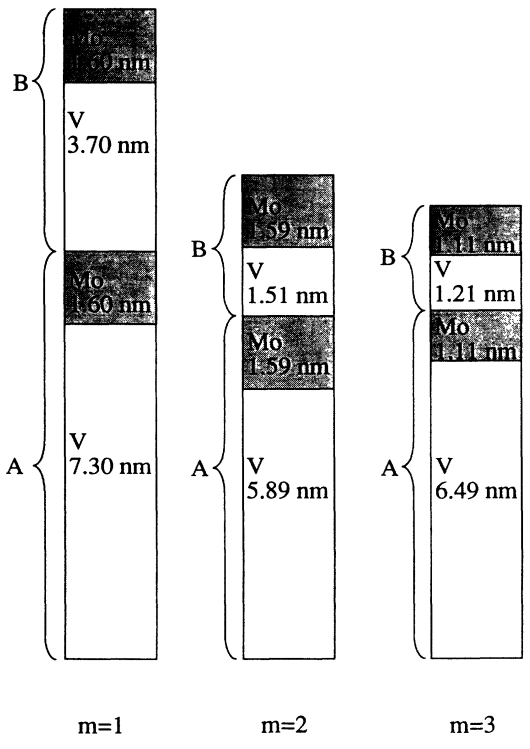

FIG. 2. Schematic representation of the two building blocks, A and B, used to realize the superlattices. Each of the two building blocks, A and B, consists of two sublayers of different materials, Mo and V. The individual layer thicknesses of the grown superlattices with different m values are shown in the figure.

which is equivalent to using the concurrent inflation rule $A \rightarrow A^m B$ and $B \rightarrow A$. To assure that two layers of the same material are not deposited next to each other, the generated sequence consists of two building blocks, A and B, each divided into two sublayers of different materials, in the present work Mo and V, respectively.

Quasiperiodic Mo/V superlattices were grown using m values of 1, 2, and 3. In these superlattices the ratios between the number of A and B blocks are given by the golden mean $\gamma(1)$, silver mean $\gamma(2)$, and bronze mean $\gamma(3)$, respectively. The layer thicknesses have been chosen according to Eq. (2.15) so Eq. (2.19) could be used for analytical predictions of the superlattice peaks positions in the diffraction spectra. Figure 2 shows a schematic representation of the building blocks with the individual layer thicknesses of each superlattice. The films were grown to a total thickness of 1 μm.

Cross-sectional transmission electron microscopy (XTEM) and SAED studies were performed by using a Philips EM400T electron microscope operated at 120 kV and the high-resolution work was carried out using a JEOL 4000EX microscope operated at 400 kV. The incident electron beam was directed along the [110] zone axis of the film. The sample-preparation technique for XTEM of thin films described by Ref. 23 was used. The final thinning of the specimen was done by ion-beam milling.

For the x-ray analyses, a wide-range goniometer with a

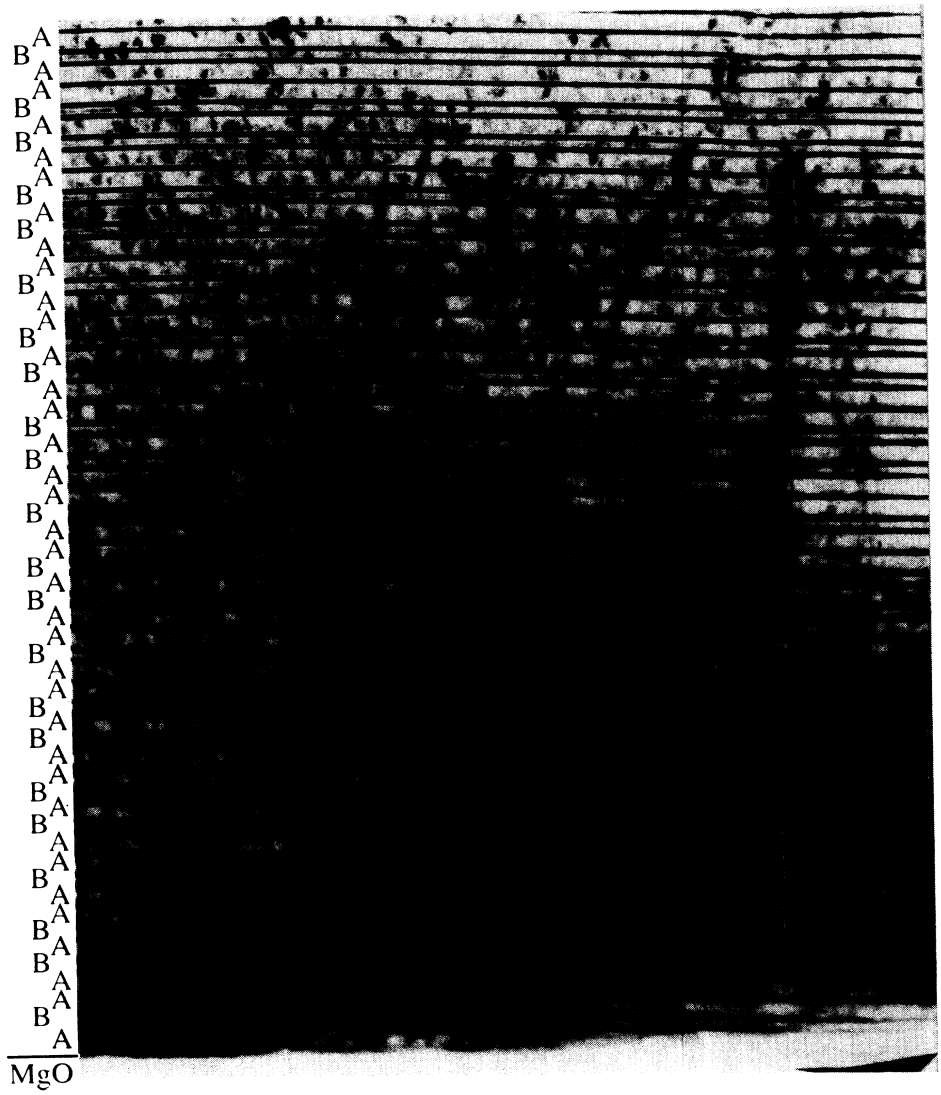

FIG. 3. Transmission electron micrograph showing the first 59 layers of the $m=1$ (Fibonacci) superlattice, the thick and thin V layers (bright), each accompanied by a Mo layer (dark), corresponds to the A and B blocks (shown in Fig. 2), respectively.

proportional detector was used and the accuracy in 2θ was 0.01°. Unmonochromized Cu radiation containing both characteristic $K\alpha_1$ and $K\alpha_2$ radiation was used and the peaks corresponding to the $K\alpha_2$ line were numerically stripped from the spectra using a Philips APD 1700 software package.

IV. RESULTS AND DISCUSSION

The $m=1$ (Fibonacci) superlattice was investigated both by conventional and high-resolution XTEM and by SAED. In the bright-field XTEM image shown in Fig. 3, the MgO substrate and the first 59 layers of the superlattice can be seen, verifying the modulation corresponding to the concurrent inflation rule $A \rightarrow AB$ and $B \rightarrow A$. The thick and thin V layers (bright), each accompanied by a thinner Mo layer (dark), corresponds to the A and B blocks, respectively, as shown in Fig. 2. A few threading dislocations which originate at the substrate-film interface can also be seen.

SAED patterns from the MgO substrate, the

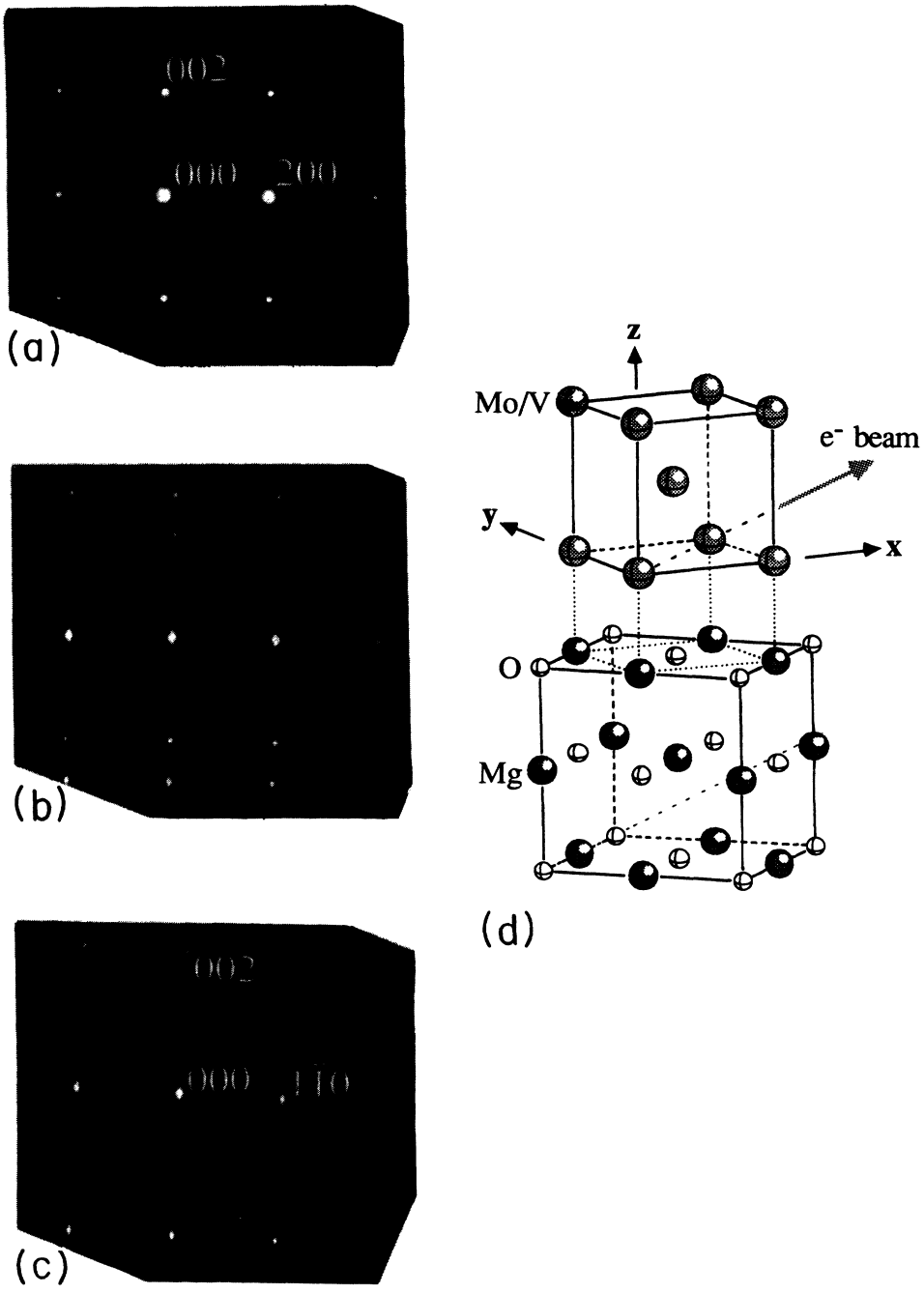

FIG. 4. SAED patterns from (a) the MgO substrate, (b) the substrate-film interface, and (c) the superlattice. In (d), the orientation of the epitaxial film is shown schematically.

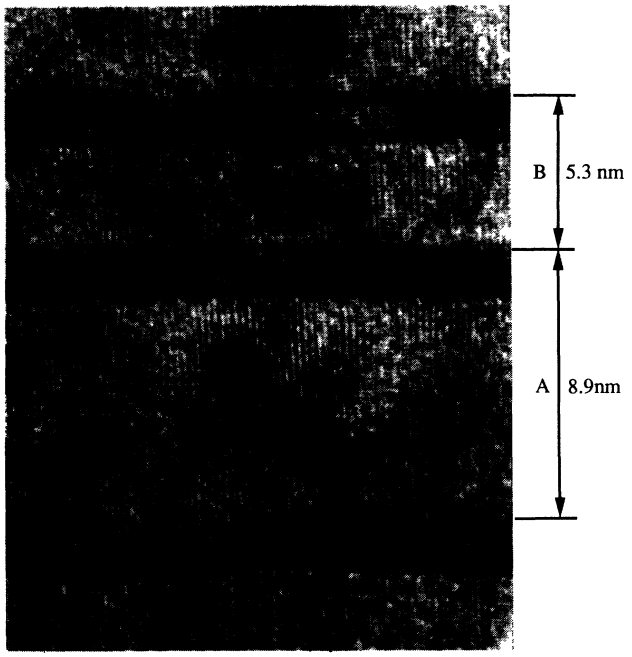

FIG. 5. High-resolution XTEM micrograph of the $m=1$ superlattice close to optimum defocus showing one A and one B block where the MO layers appear darker due to higher atomic number. The (002) and (110) lattice fringes, which are parallel and perpendicular to the superlattice layers, respectively, are clearly resolved. The average interface width is estimated to be two (002) lattice plane spacings (≈ 0.31 nm).

substrate-film interface, and the superlattice are shown in Figs. 4(a)–4(c). The patterns show that the film is grown with a 45° rotation around the surface normal of the substrate as shown schematically in Fig. 4(d). Since no change of the SAED pattern was observed when the selected area aperture (diameter ≈ 1 μm) was moved along the film, it can be concluded that the film is single crystalline.

A high-resolution XTEM micrograph of the superlattice is shown in Fig. 5. Lattice fringes which are parallel

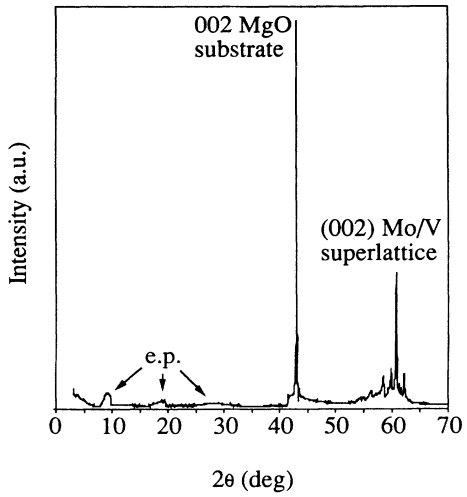

FIG. 6. Overview of x-ray θ-2θ spectrum from the $m=1$ superlattice. The peaks labeled e.p. are due to escape-peak phenomena of the x-ray detector.

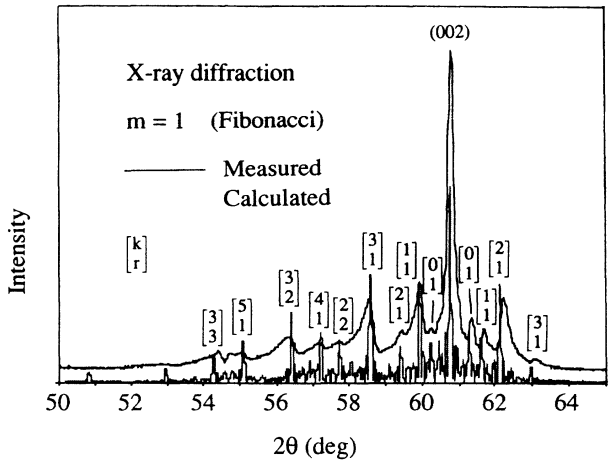

FIG. 7. Experimental and numerically calculated x-ray θ-2θ spectra from the Fibonacci ($m=1$) superlattice. Analytically predicted peaks are labeled with the corresponding indices $[^k_r]$.

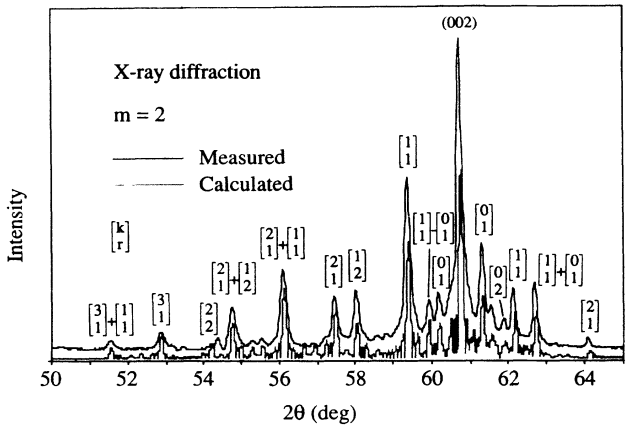

FIG. 8. Experimental and numerically calculated x-ray θ-2θ spectra from the $m=2$ superlattice. Analytically predicted peaks are labeled with the corresponding indices $[^k_r]$.

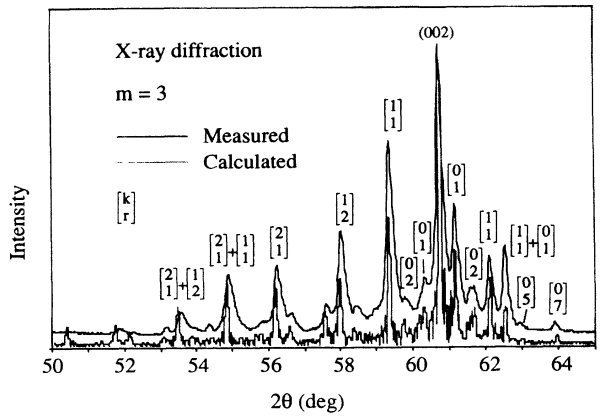

FIG. 9. Experimental and numerically calculated x-ray θ-2θ spectra from the $m=3$ superlattice. Analytically predicted peaks are labeled with the corresponding indices $[^k_r]$.

and perpendicular to the superlattice layers correspond to (002) and (110) lattice planes, respectively. The interfaces between the Mo (dark) and V layers (bright) are locally atomically sharp but over a larger area steps in the $\pm$[002] direction are observed. The average interface width is estimated to be two (002) planes ($\approx$0.31 nm). The relatively sharp interfaces obtained are, we believe, due to a negligible bulk diffusion but a relatively high surface diffusion at 700 °C in combination with a fast shutter mechanism and the interruption of the film growth for 0.25 s between each layer. The latter allows the surface of the growing film to relax between each deposited layer. The steps of ± 1 [002] lattice plane is most probably due to deposition of incomplete layers. Although such a smearing of the interfaces with ± 1 lattice plane will be visible in the calculated diffraction spectra, the effect will only be slightly decreased intensities of the satellite peaks.[21] The assumption that the interfaces are atomically sharp is thus sufficient for reliable numerical calculations of the diffraction peaks is described in Sec. II.

X-ray θ-2θ spectra were taken in the small- as well as the high-angle regions from the superlattices with $m=1$, 2, and 3, however the spectra always showed a much richer superlattice structure in the high-angle region, which is evident in the overview spectrum from a Fibonacci ($m=1$) superlattice shown in Fig. 6. For this reason we limited the calculations of the XRD spectra to this region. Figures 7–9 show the experimental and numerically calculated spectra for different m values together with the analytically predicted peaks, which are marked and assigned with their indices $[^k_r]$ according to Eq. (2.19).

The agreement is striking and best for the silver-mean and copper-mean superlattices which might indicate that they have shaper interfaces or smaller fluctuations in layer thicknesses than the golden mean superlattice. Notable also is that the largest peaks seem to appear in a more periodic way for larger m values. This can be understood intuitively by considering the quasiperiodic superlattices as periodic repetitions of A blocks interrupted by single B blocks at positions determined by the quasiperiodic sequence used. The numbers of consecutive A blocks will be m or $m+1$, and in the limit when $m \rightarrow \infty$ a superlattice with a finite thickness will become periodic. The true quasiperiodic wavelengths were found to deviate from the desired Λs by as much as 15% determined by fitting the calculated spectra to the experimental spectra. This deviation may be explained by target erosion and small fluctuations in the pressure that affect the deposition rates, which in turn also leads to deposition of incomplete layers and therefore smeared interfaces.

The SAED pattern of Fig. 10, which is the same as in Fig. 4(c) but obtained with a larger camera length, shows a large number of superlattice reflections around the (000) and (002) Mo/V reflections. In the intermediate part, with low intensity, the pattern was further exposed to increase the resolution. Some intensity can be seen all the way between the (000) and (002) reflections, which is due to the fact that quasiperiodic superlattices have infinitely many satellites between two major reflections. A densitometer recording of the pattern together with a numerically calculated spectrum is shown in Figs. 11(a) and 11(b) and the analytically predicted peaks are marked at their positions and assigned with indices $[^k_r]$ according to Eq. (2.19). The densitometer scan of the (000) satellites was made on the normally exposed side of the primary beam in order to achieve as true intensity distribution as possible. A very good agreement between the analytically calculated, the numerically calculated, and the SAED pattern can be seen for the peak positions. However, the intensity distribution of the satellites does not fit as well

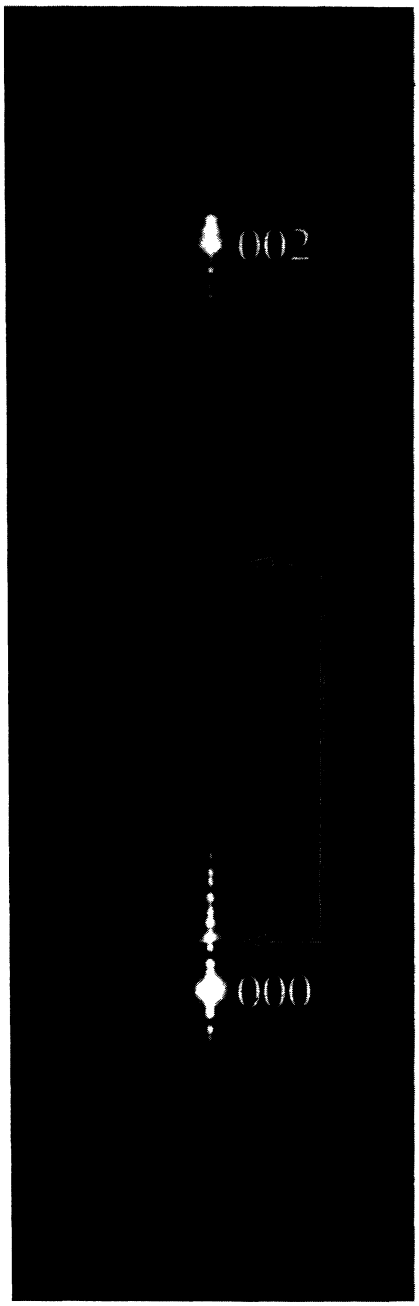

FIG. 10. SAED pattern showing the (000) and (002) Mo/V reflections and the superlattice satellites. The part of the diffractogram which is marked with arrows has partly been further exposed in order to resolve as many peaks as possible.

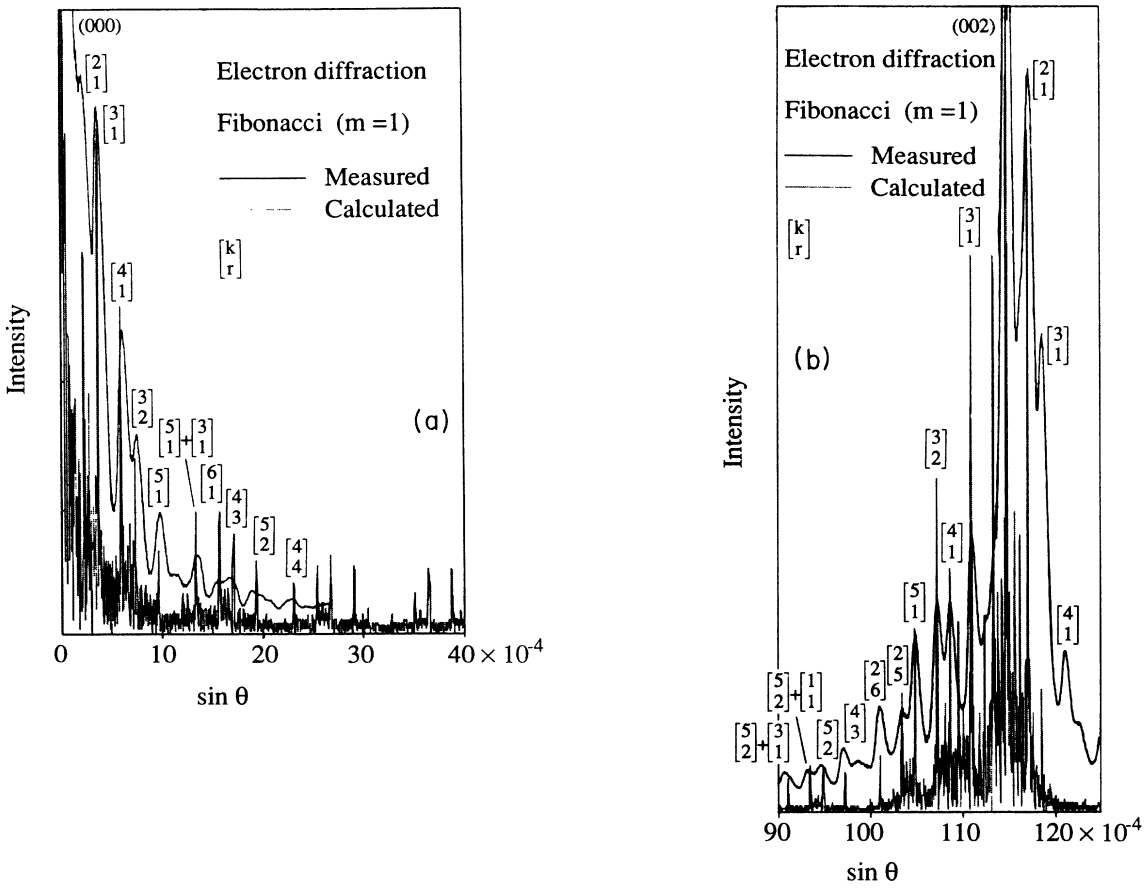

FIG. 11. The intensity distribution of the diffractogram of Fig. 10 together with the numerically calculated spectra. (a) and (b) show the satellites around the (000) and (002) Mo/V reflections, respectively. The position of the analytically predicted peaks are marked and indexed with their respective $[^k_r]$.

as in the case of XRD, which may be due to several artifacts, such as dynamic effects during electron diffraction, nonlinear intensity response of the photographic plate, imperfect interfaces, and small fluctuations in the layer thicknesses.

To summarize, the present work shows that dual target dc magnetron sputtering can be used for preparation of high-quality single-crystalline Mo/V superlattices. A fast computer-controlled shutter mechanism enables the growth of superlattices with sharp interfaces and well-defined (quasiperiodic) orders. Furthermore for precious means quasiperiodic sequences obtained by the concurrent inflation rule $A \rightarrow A^m B$ and $B \rightarrow A$, the largest satellite peaks in XRD and SAED are analytically shown to occur for scattering vectors $q = 2\pi\Lambda^{-1} r[\gamma(m)]^k$, where r and k are integers, Λ is an average superlattice wavelength, and $\gamma(m) = \frac{1}{2}[m + (m^2+4)^{1/2}]$, provided that the ratio of the thickness of the building blocks A and B is chosen to be $\gamma(m)$. This result is verified for $m = 1$, 2, and 3 both by experimental and numerically calculated spectra.

ACKNOWLEDGMENTS

Financial support from the STUF branch of the Swedish Board for Technical Development is highly appreciated.

*Permanent address: Nippon Sheet Glass Company, Ltd., 5-4 Tokodai, Tsukuba-city, Ibaraki Pref. 300-26, Japan.

†On leave of absence from Research Institute for Technical Physics, P.O. Box 76, H-1325 Budapest, Hungary.

[1] M. R. Kahn, C. S. L. Chun, G. P. Felcher, M. Grimsditch, A. Kuney, C. M. Falco, and I. K. Schuller, Phys. Rev. B **27**, 7186 (1983).

[2] A. Hu, S. Zhang, X. Yuan, Q. Shen, Z. Lu, and D. Feng, Phys. Status Solidi A **107**, 153 (1988).

[3] J. L. Makous and C. M. Falco, Solid State Commun. **68**, 375

(1988).
[4]M. T. Pérez-Frías and J. L. Vicent, Phys. Rev. B **38**, 9503 (1988).
[5]U. Helmersson, S. Todorova, L. Markèrt, S. A. Barnett, J.-E. Sundgren, and J. E. Greene, J. Appl. Phys. **62**, 481 (1987).
[6]J. M. Murduck, D. W. Capone, I. K. Schuller, S. Foner, and J. B. Ketterson, Appl. Phys. Lett. **52**, 504 (1988).
[7]F. Capasso, K. Mohammed, and A. E. Cho, IEEE J. Quantum Electron. **QE-22**, 1853 (1986).
[8]R. Merlin, IEEE J. Quantum Electron. Quantum Well Heterostruct. Superlatt. (to be published).
[9]D. Shechtman, I. Blech, D. Gratias, and J. W. Cahn, Phys. Rev. Lett. **53**, 1951 (1984).
[10]D. Levine and P. J. Steinhardt, Phys. Rev. B **34**, 596 (1986).
[11]R. Merlin, K. Bajema, R. Clarke, F.-Y. Juang, and P. K. Bhattacharya, Phys. Rev. Lett. **55**, 1768 (1985).
[12]M. G. Karkut, J.-M. Triscone, D. Ariosa, and Ø. Fisher, Phys. Rev. B **34**, 4390 (1986).
[13]R. Riklund and M. Severin, J. Phys. C **21**, 3217 (1988).
[14]M. Severin, J. Phys. Condens. Matter **1**, 6771 (1989).
[15]G. Gumbs and M. K. Ali, J. Phys. A **21**, L517 (1988).
[16]M. Kolář and M. K. Ali, J. Phys. Condens. Matter **1**, 823 (1989).
[17]R. Riklund, M. Severin, and Y. Liu, Int. J. Mod. Phys. B **1**, 121 (1987).
[18]R. Merlin, K. Bajema, J. Nagle, and K. Ploog, J. Phys. (Paris) Colloq. **48**, C5-503 (1987).
[19]Y. Fujii, in *Metallic Superlattices,* edited by T. Shinjo and T. Takada (Elsevier, Amsterdam, 1987), p. 44.
[20]J. P. Lu and J. L. Birman, J. Phys. C **3**, 251 (1986).
[21]J. Birch, G. Radnoczi, L. Hultman, G. Håkansson, U. Wahlström, Y. Yamamoto, J. E. Sundgren, and L. R. Wallenberg, unpublished.
[22]J. P. Lu, T. Odagaki, and J. L. Birman, Phys. Rev. B **33**, 4809 (1986).
[23]C. F. Gong, H. T. G. Hentzell, A. Robertsson, and G. Radnoczi, IEE Proc. **137**, 53 (1990).

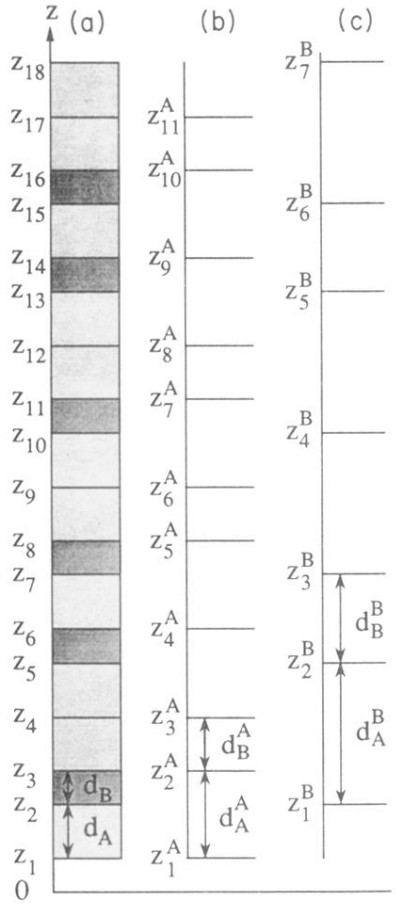

FIG. 1. Schematic representation of (a) the superlattice where $d_{A\,(B)}$ represents the thicknesses of the A and B building blocks and z_n are their positions according to Eq. (2.2). (b) and (c) show the two sublattices formed by the positions, z_n^A and z_n^B, of the A and B building blocks, respectively. The only difference between the A and B sublattices is their lattice constants $d_{A\,(B)}^A$ and $d_{A\,(B)}^B$, respectively.

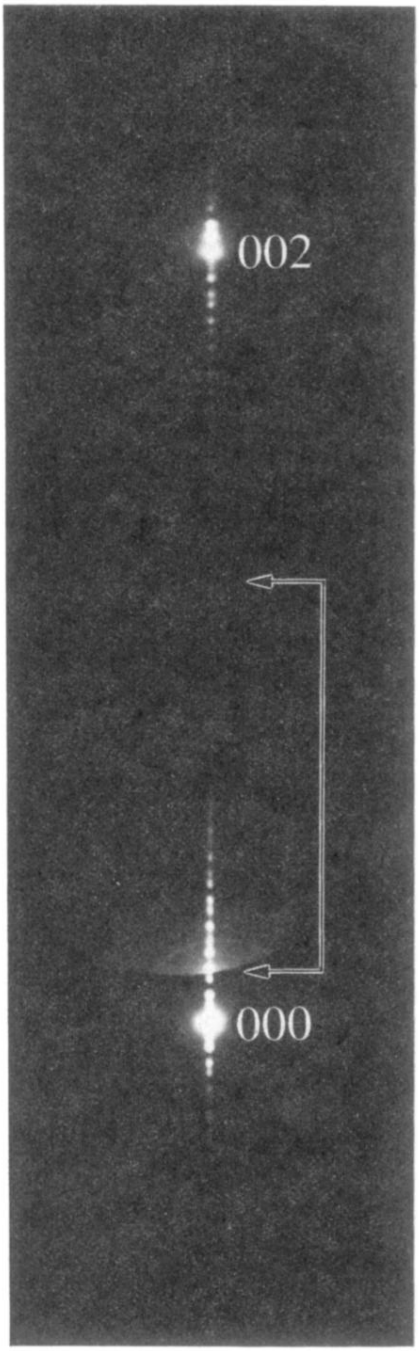

FIG. 10. SAED pattern showing the (000) and (002) Mo/V reflections and the superlattice satellites. The part of the diffractogram which is marked with arrows has partly been further exposed in order to resolve as many peaks as possible.

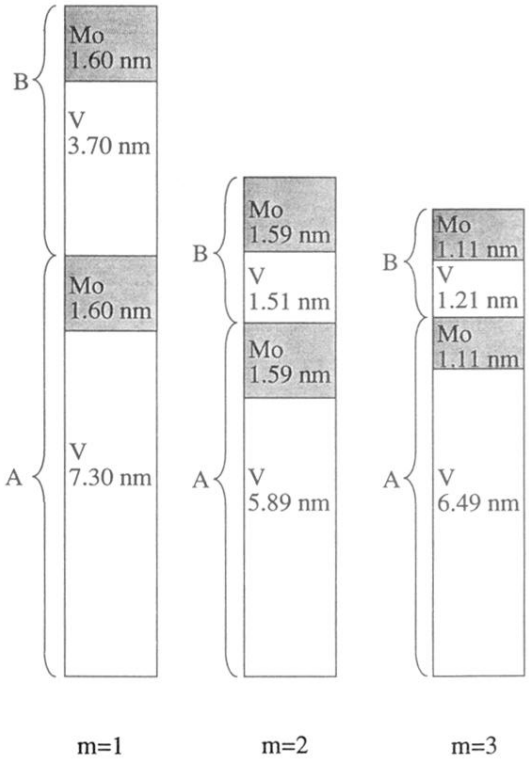

FIG. 2. Schematic representation of the two building blocks, *A* and *B*, used to realize the superlattices. Each of the two building blocks, *A* and *B*, consists of two sublayers of different materials, Mo and V. The individual layer thicknesses of the grown superlattices with different *m* values are shown in the figure.

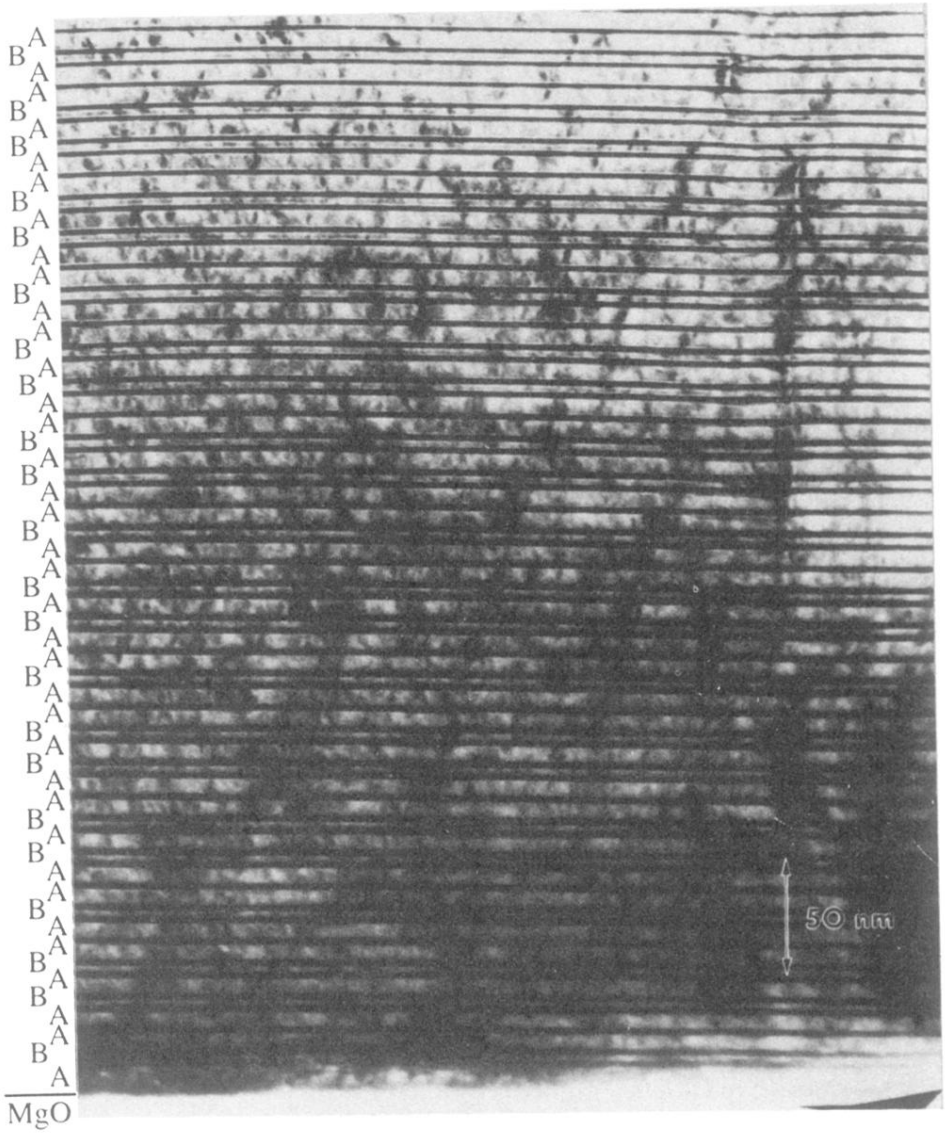

FIG. 3. Transmission electron micrograph showing the first 59 layers of the $m=1$ (Fibonacci) superlattice, the thick and thin V layers (bright), each accompanied by a Mo layer (dark), corresponds to the A and B blocks (shown in Fig. 2), respectively.

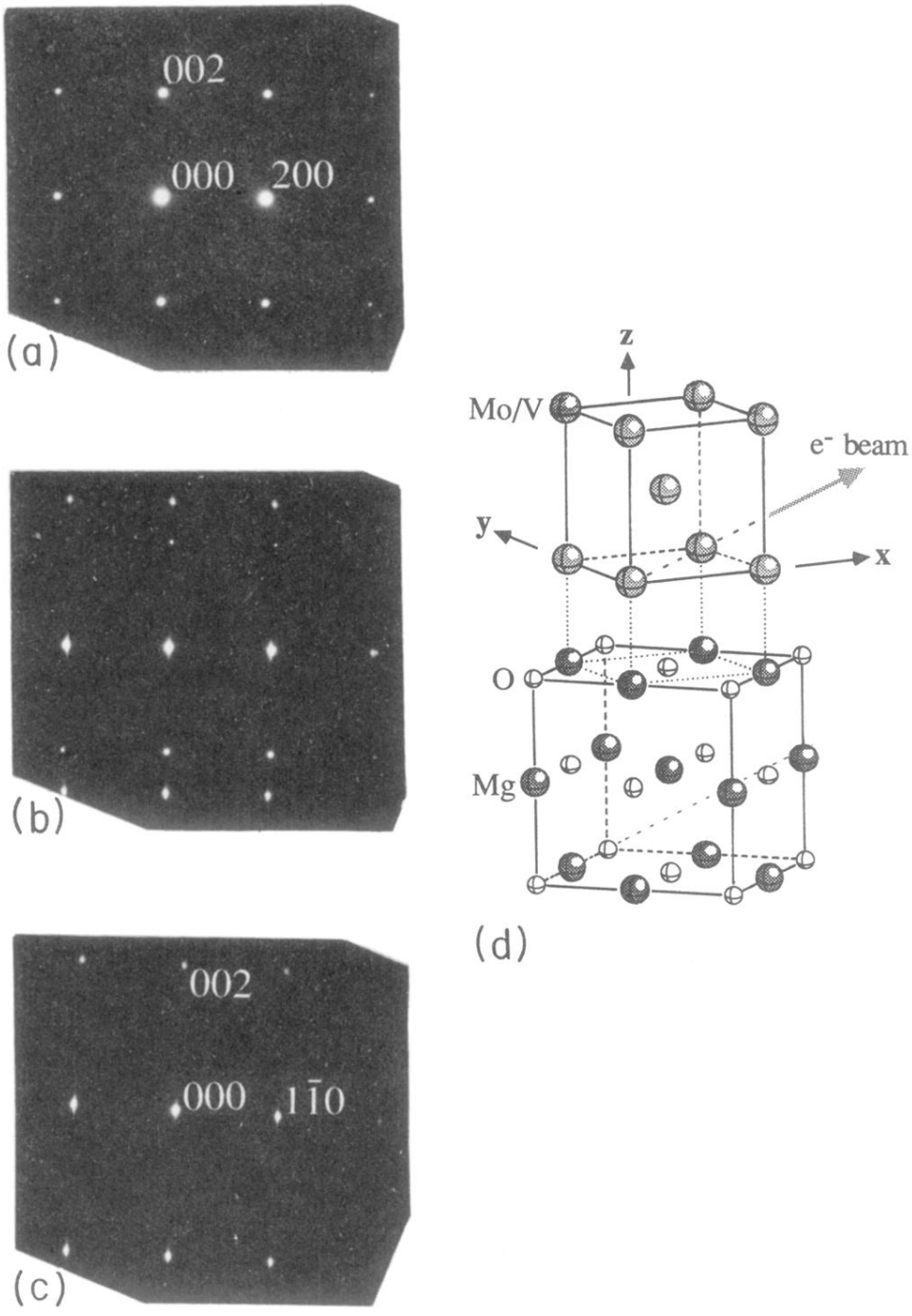

FIG. 4. SAED patterns from (a) the MgO substrate, (b) the substrate-film interface, and (c) the superlattice. In (d), the orientation of the epitaxial film is shown schematically.

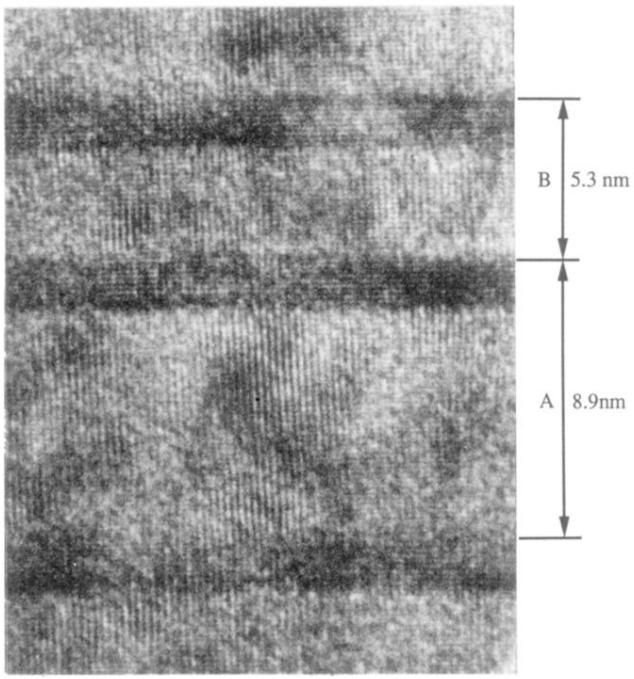

FIG. 5. High-resolution XTEM micrograph of the $m=1$ superlattice close to optimum defocus showing one *A* and one *B* block where the MO layers appear darker due to higher atomic number. The (002) and (110) lattice fringes, which are parallel and perpendicular to the superlattice layers, respectively, are clearly resolved. The average interface width is estimated to be two (002) lattice plane spacings (≈ 0.31 nm).